ARTICLE

Direct Imaging of the Structure, Relaxation, and Sterically Constrained Motion of Encapsulated Tungsten Polyoxometalate Lindqvist Ions within Carbon Nanotubes

Jeremy Sloan,[†,‖,*] Gemma Matthewman,[‡] Clare Dyer-Smith,[‡] A-Young Sung,[§] Zheng Liu,[⊥] Kazu Suenaga,[⊥] Angus I. Kirkland,[‖] and Emmanuel Flahaut[#]

[†]Queen Mary, University of London, Department of Engineering and Materials, Mile End Road, London, E1 4NS, U.K., [‖]Department of Materials, University of Oxford, Parks Road, Oxford, OX1 3PH, U.K., [‡]Inorganic Chemistry Laboratory, University of Oxford, South Parks Road, Oxford OX1 3QW, U.K., [§]School of Health Sciences, Daebul University, Chonnam 526-702, South Korea, [⊥]National Institute for Advanced Industrial Science and Technology (AIST), Research Centre for Advanced Carbon Materials, Tsukuba, Ibaraki 3058565, Japan, and [#]Université Paul Sabatier, UMR CNRS 5085 Bât. 2RI 31062 Toulouse Cedex 9, France

ABSTRACT The imaging properties and observation of the sterically regulated translational motion of discrete tungsten polyoxometalate Linqvist ions (*i.e.*, $[W_6O_{19}]^{2-}$) within carbon nanotubes of specific internal diameter are reported. The translational motion of the nonspheroidal anion within the nanotube capillary is found to be impeded by its near-perfect accommodation to the internal van der Waals surface of the nanotube wall. Rotational motion of the anion about one remaining degree of freedom permits translational motion of the anion along the nanotube followed by locking in at sterically favorable positions in a mechanism similar to a molecular ratchet. This steric locking permits the successful direct imaging of the constituent octahedral cation template of individual $[W_6O_{19}]^{2-}$ anions by high resolution transmission electron microscopy thereby permitting meterological measurements to be performed directly on the anion. Direct imaging of pairs of equatorial W_2 atoms within the anion reveal steric relaxation of the anion contained within the nanotube capillary relative to the bulk anion structure.

KEYWORDS: polyoxometalate · Lindqvist ion · tungsten · carbon nanotubes · electron microscopy

*Address correspondence to j.sloan@qmul.ac.uk.

Received for review September 22, 2007 and accepted March 27, 2008.

Published online May 6, 2008.
10.1021/nn7002508 CCC: $40.75

Carbon nanotubes have proven to be effective templates for the precise engineering of materials on a subnanometer scale and a wide variety of one-dimensional (1D) crystal structures including multiples of polymeric iodine chains,[1,2] reduced coordination $2 \times 2 \times \infty$ or $3 \times 3 \times \infty$ atomic-layer-thick KI crystals,[3,4] polyhedral chains of lanthanide trihalides,[5,6] encapsulated tubules or 1D chains of ice crystals,[7,8] twisted 1D Co_2I_4 double chains,[9] a new trigonal tubular form of HgTe,[10] and reduced coordination polymorphs of PbI_2[11] have either been calculated and/or directly observed to form within the interior of single- or double-walled carbon nanotubes (SWNTs or DWNTs). Parallel studies have shown that nanotube-encapsulated molecular structures such as 1D close-packed chains of C_{60}[12] endofullerenes[13,14] or functionalized fullerenes[15] and other molecular species including metallocenes,[16–18] Zn-diphenylporphyrin,[19] *ortho*-carborane,[20] uranyl acetate,[21] and octasiloxane,[22] can be directly imaged using either high resolution transmission electron microscopy (HRTEM) or scanning transmission electron microscopy (STEM). When periodic crystalline materials are imaged within SWNTs, HRTEM can be used to study their crystal structures in considerable detail.[1–11] However, because of their tendency to move rapidly or rearrange in an electron beam (see below), it is comparatively difficult to perform similarly detailed structural studies on encapsulated discrete molecules.

Within a HRTEM or a STEM, nanotube-encapsulated species are imaged in a two-dimensional projection at a spatial resolution of ~0.16 nm although direct or indirect aberration correction can produce images at a spatial resolution close to 0.1 nm.[23–27] Limitations on the interpretability of images of the encapsulated materials are then set by the electron scattering power of the constituent atoms, the specimen thickness, the superposition of the encapsulating nanotube over the encapsulated species, and the relative stability of the confined species in the imaging electron beam. For molecules, further considerations must be made with

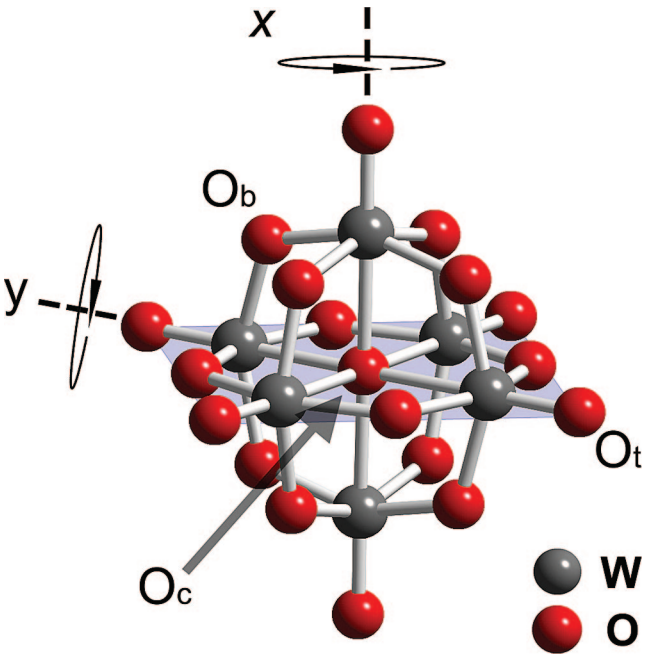

Figure 1. The $[W_6O_{19}]^{2-}$ polyoxometalate Lindqvist anion showing terminal (O_t), bridging (O_b), and central (O_c) oxygen atoms. The vertical (*x*) and horizontal (*y*) axes of rotation used in HRTEM image simulations in Figure 2 are indicated. The equatorial plane orthogonal to the *x*-axis of rotation is also shaded in gray.

regard to their dynamical motion and stability in an electron beam.[13–22] Spheroidal molecules such as fullerenes, endofullerenes, and carborane rotate at room temperature in the solid state, even in the absence of an electron beam,[28] and can disintegrate or coalesce when irradiated.[12] The often poor steric match of the encapsulated molecules to the internal surface of the encapsulating nanotube also results in motion during electron beam irradiation. As a result of this steric mismatch, the walls of encapsulated fullerenes,[12] functionalized fullerenes,[15] and endofullerenes[13,14] are often not rigidly fixed. The observation of *in situ* rotation of functional groups within functionalized fullerenes[15] and the dynamical motion of encapsulated metal atoms observed within endofullerenes[13,14] give further evidence for this. In this paper we describe both simulated and experimental imaging of $[W_6O_{19}]^{2-}$ Lindqvist ions within nanotubes which, because of their nonspheroidal shape, can lock into place within the capillaries of nanotubes with specific internal diameter, allowing the constituent W_6 cation framework to be imaged directly by HRTEM.

Polyoxometalates (POMs) are part of a diverse family of cluster anions formed in solution by self-assembly oligomerization processes from edge- or corner-sharing arrangements of octahedral

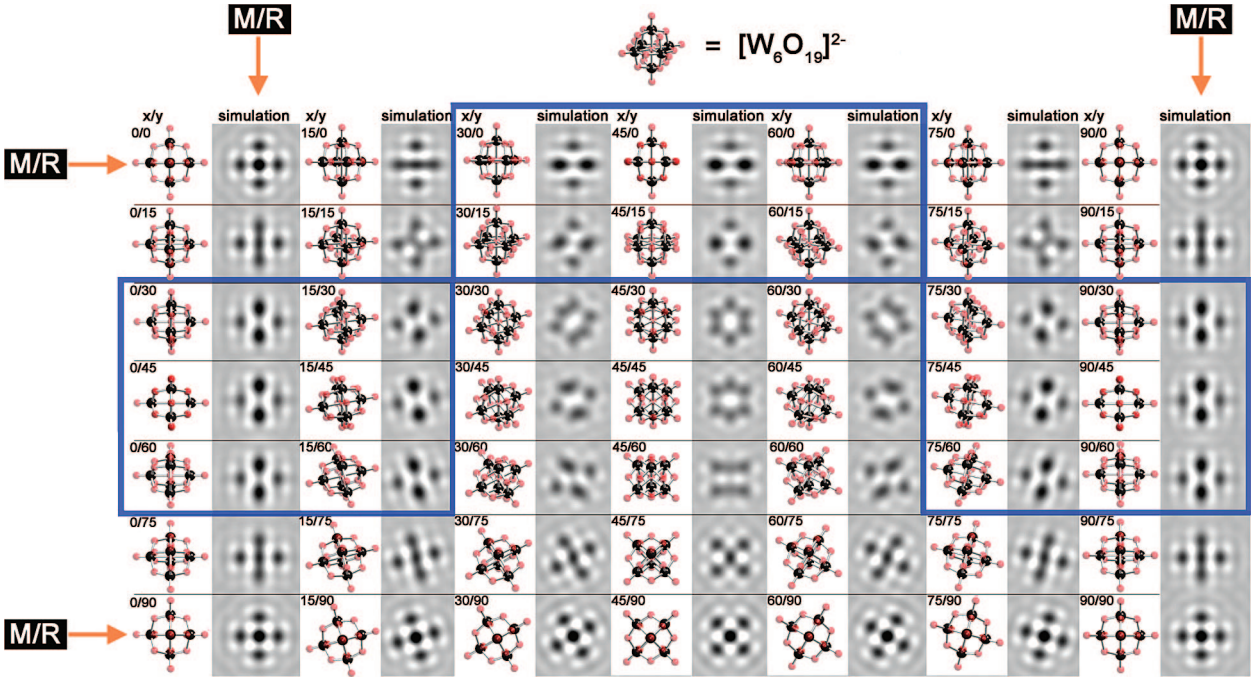

Figure 2. Tableau of structure models (left in each column) and corresponding HRTEM image simulations (right in each column) calculated for the Scherzer defocus (−34 nm) corresponding to the $[W_6O_{19}]^{2-}$ anion viewed in different *x*/*y* orientations (axes *x* and *y* defined in Figure 1). The 19 oxygen atoms were included in the simulation calculations but the contrast is dominated by the W_6 cation framework, with the O_{19} anion framework giving only a weak diffuse contribution (see also Figure 4d). This tableau includes only a partial subset of all possible orientations of the cluster anion; the remainder may be reproduced from mirror plane (M) and rotational (R) symmetry operations produced with respect to the M/R directions indicated at the borders of the figure. The blue boxes indicate *x*/*y* projections either equivalent or nearly equivalent to the experimentally observed image contrast (see Figures 3, 4, and 7). The equivalent projections indicated by the bounding blue boxes are those which give contrast similar to the experimental images reproduced in Figures 3 and 4.

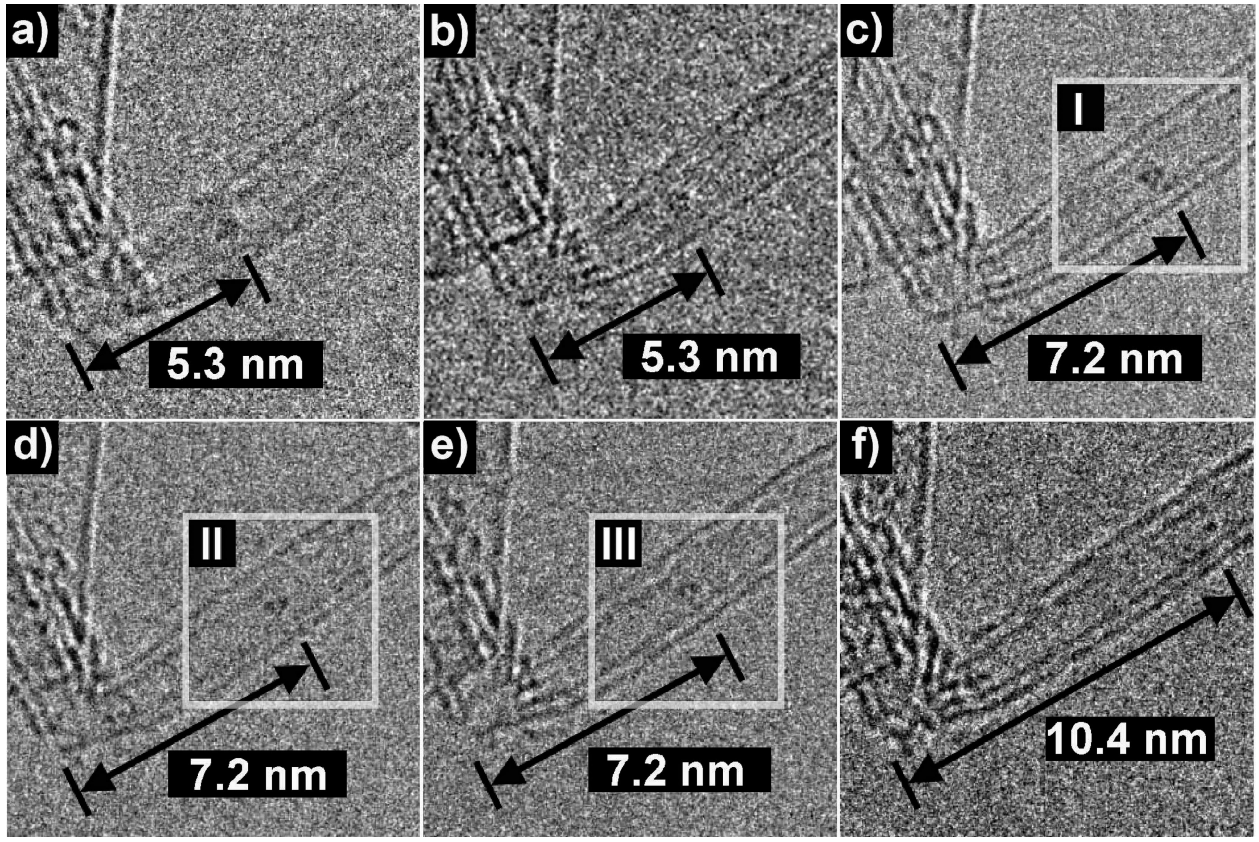

Figure 3. (a–f). Sequence of unprocessed HRTEM images of a discrete $[W_6O_{19}]^{2-}$ polyoxometalate anion within a DWNT obtained at various time intervals (given in the text). The indicated distances correspond to the physical distance of the estimated centre of gravity of the anion from the bend in the DWNT on the left in each micrograph.

MO_6 ((M) = V, Nb, Ta, Mo or W), or from mixtures of these cations with other transition metal, main group or lanthanide elements.[29–32] In general they form either superpolyhedral or cage-like structures including the Keggin-type (*e.g.*, $[(PW_{12}O_{40}]^{3-}$),[33] Wells-Dawson-type (*e.g.*, $(K_{28}H_8[P_2W_{15}Ti_3O_{60.5}]_4)$)[34] or the Preyssler-type (*e.g.*, $[NaP_5W_{30}O_{11}0]^{14-}$)[35] polyoxoanions which are prepared in conjunction with either simple organic counterions[33,36] or more complex species, for example dendrons.[37] POMs have significant biochemical activity and can inhibit electron transport and DNA polymerase, a feature that makes them potentially suitable as anti-HIV agents.[38] They are also useful in catalysis to promote oxidation of alcohols and epoxidation of alkenes[39] and can behave as molecular magnets which have been proposed as spin qbits for quantum computation.[40,41]

One of the simplest polyoxometalates is the so-called Linqvist anion in which six MO_6 octahedra combine to form a superoctahedron of the form $[M_6O_{19}]^{2-}$ (M = Nb, Ta, Mo, and W) with O_h symmetry, as shown for M = W in Figure 1.[36,42,43] In the resulting structure, the W atoms are separated by three types of oxygen linkages: terminal (O_t in Figure 1), bound to one metal atom (μ_1); bridging (O_b in Figure 1), bridging two metal atoms (μ_2); and central (O_c in Figure 1), at the center of an octahedral arrangement of metal atoms as exhibited by a solid oxide lattice (μ_6). The W^{VI} $[W_6O_{19}]^{2-}$ Lindqvist anion is both thermally stable and radiation resistant and, we find, suitable for HRTEM investigation. In the present study, this anion is prepared in conjunction with the counterion $[n\mathrm{Bu}_4\mathrm{N}]^+$ as $[W_6O_{19}][n\mathrm{Bu}_4\mathrm{N}]_2$[36] and then inserted into DWNTs or SWNTs from nonaqueous solution.[44]

RESULTS AND DISCUSSION

In conventional HRTEM images, the contrast of single $[W_6O_{19}][n\mathrm{Bu}_4\mathrm{N}]_2$ molecules will be dominated by the six strongly scattering W ($Z = 74$) atoms in the $[W_6O_{19}]^{2-}$ superoctahedron while the nineteen weaker scattering O ($Z = 8$) atoms will give rise to comparatively diffuse contrast. Individual $[n\mathrm{Bu}_4\mathrm{N}]^+$ species will also give rise to comparatively diffuse contrast due to the low atomic numbers of C ($Z = 6$), N ($Z = 7$), and H ($Z = 1$). For imaging and simulation purposes, we have therefore not considered the effects of the $[n\mathrm{Bu}_4\mathrm{N}]^+$ counter-ions directly but, assume their presence in close proximity to the anion in order to maintain charge neutrality.

HRTEM images for the $[W_6O_{19}]^{2-}$ anion in various projections at the Scherzer defocus were computed according to the multislice algorithm[45,46] using parameters typical for our instrument, as shown in Figure 2, assuming perfect O_h symmetry for the anion. In this fig-

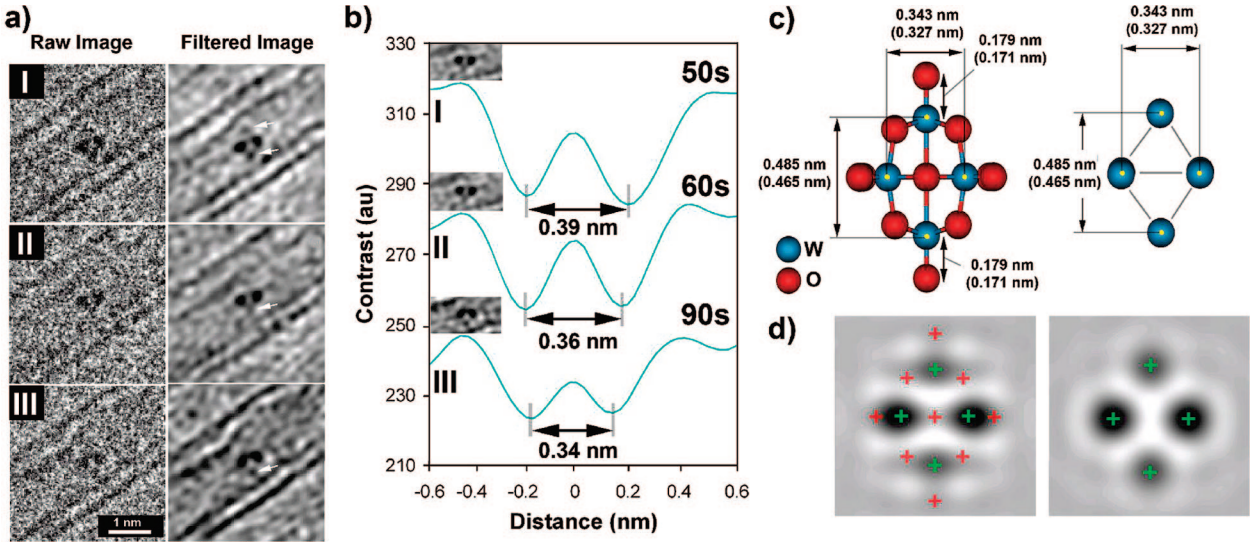

Figure 4. (a) Details I–III (left) obtained from the indicated regions of the raw images in Figure 3 panels c–e shown side-by-side with corresponding Fourier-filtered images (right); (b) line profiles produced through the equatorial spots corresponding to W_2 atom pairs with the spot separations indicated; (c) structure models of the $[W_6O_{19}]^{2-}$ anion in an *x*/*y* orientation (as defined in Figures 1 and 2) of 45/0 both with oxygen (left) and with oxygen excluded (right). Selected atom–atom distances are included for the unrelaxed anion (in brackets) and the relaxed anion. (d) Image simulations calculated at the Scherzer defocus using the structure models in panel c showing the effect of including oxygen in the image simulation calculation. When the oxygens are included (left simulation), the centre of the contrast due to the equatorial W_2 atom pairs is distorted outward towards the three terminal oxygen atoms. When the oxygens are not included, there is relatively little distortion. In both simulations, the apical single W atom positions are not distorted by the presence or absence of oxygen. Red crosses (O) and green crosses (W) are shown as a guide.

ure a tableau of image simulations is shown for a single $[W_6O_{19}]^{2-}$ anion rotated at 15° intervals about its vertical axis (*x* in Figure 1) and its horizontal axis (*y* in Figure 1) relative to an arbitrary starting orientation in which the electron beam direction is defined along an axial pair of W atoms within the W_6 octahedral framework (parallel to *x*, Figure 1). Thus, in the orientation with *x*/*y* = 0/0 (top left, Figure 2) the simulation resembles a Maltese Cross with the central dark spot corresponding to the axial pair of W atoms and the four surrounding weaker spots corresponding to individual equatorial W atoms within a W_6 cation superoctahedron. If this cluster is rotated about either the *x* or the *y* axes (from *x*/*y* = 0/0 to 90/0 or from orientation 0/0 to 0/90, Figure 2), the contrast from the four W atoms on the equatorial plane (defined orthogonal to the *x* or *y* axes; one such plane is indicated in Figure 1) smear to form a dark line (*x*/*y* = 15/0, 75/0, 0/15, 0/75 Figure 2) and then form two discrete dark spots corresponding to either a staggered pair of W atoms (*x*/*y* = 30/0, 60/0, 0/30, 0/60 Figure 2) or a pair of W atoms (*i.e.*, a W_2 column) viewed in projection (*x*/*y* = 45/0 or 0/45, Figure 2). When the anion is rotated about both the *x* and *y* axes, different contrast is obtained corresponding to the projection of the $[W_6O_{19}]^{2-}$ species relative to the incident electron beam direction. For example, at projection *x*/*y* = 45/45, six black spots are clearly visible as all six atoms can be viewed along this diagonal projection, whereas at *x*/*y* = 0/0, 90/90, *etc.*, only five spots are visible.

Figure 3panels a–f show a sequence of six experimental HRTEM images obtained at intervals over a period of *ca.* 100 s of a discrete $[W_6O_{19}]^{2-}$ anion encapsulated within a DWNT with a measured outer diameter of 2.03 nm and inner diameter of 1.21 nm. In the initial image (Figure 3a and an image taken 32 s later (Figure 3b), the $[W_6O_{19}]^{2-}$ anion is visible with indistinct contrast located 5.3 nm from a bend in the DWNT. In Figure 3c, taken after 50 s, Figure 3d, taken after 60 s, and Figure 3e, taken after 90 s, the anion has moved along the tube to a fixed position 7.2 nm from the bend in the DWNT. In these images, the W_6 cation template is clearly resolved and appears to be beam stable for a period of *ca.* 40 s. After a total elasped time of 100 s, the anion moves to a position 10.4 nm from the bend in the DWNT. Enlarged details **I**, **II**, and **III**, from Figure 3 panels c–e, (Figure 4a, left) show in detail the image contrast due principally to the W_6 cation template of the $[W_6O_{19}]^{2-}$ anion. Figure 4a right shows corresponding filtered versions of the same images obtained by applying an identical adaptive filter to Fourier transforms obtained from each of the details **I**–**III**. In both sets of images, the image contrast due to the $[W_6O_{19}]^{2-}$ anion consists of a spot configuration consistent with an *x*/*y* orientation equivalent to *ca.* 45/0. (Note that for a $[W_6O_{19}]^{2-}$ anion with perfect O_h symmetry, there are a number of other equivalent projections to *x*/*y* = 45/0, including 0/45, 90/45, and other projections tilted about *x* and/or *y* slightly away from these ideal projections as indicated by the bounding blue boxes in the Figure 2; *x*/*y* projections outside the indicated boxes clearly do not correspond to the experimentally observed contrast as they do not reproduce the experimentally observed spot configuration.) The most promi-

TABLE 1. Selected Bond Distances for Unrelaxed and Relaxed $[W_6O_{19}]^{2-}$ Obtained or Calculated[47] from Fragments of the Bulk Crystal Structure for $[nBu_4N]_2[W_6O_{19}]$[36a]

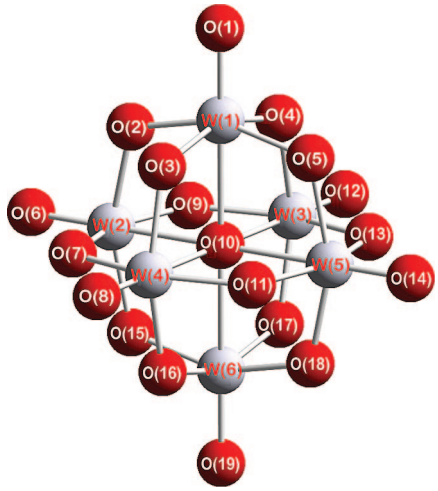

unrelaxed structure		MOPAC relaxed structure	
bond	distance (nm)	bond	distance (nm)
W(1)—O(1)	0.1708	W(1)—O(1)	0.1785
W(1)—O(2)	0.1904	W(1)—O(2)	0.2036
W(1)—O(3)	0.1931	W(1)—O(3)	0.2036
W(1)—O(4)	0.1907	W(1)—O(4)	0.2036
W(1)—O(5)	0.1887	W(1)—O(5)	0.2036
W(1)—O(10)	0.2324	W(1)—O(10)	0.2423
W(2)—O(2)	0.1937	W(2)—O(2)	0.2037
W(2)—O(6)	0.1695	W(2)—O(6)	0.1783
W(2)—O(7)	0.1907	W(2)—O(7)	0.2036
W(2)—O(9)	0.1903	W(2)—O(9)	0.2036
W(2)—O(10)	0.2309	W(2)—O(10)	0.2425
W(2)—O(15)	0.1915	W(2)—O(15)	0.2036
W(3)—O(3)	0.1923	W(3)—O(3)	0.2036
W(3)—O(7)	0.1913	W(3)—O(7)	0.2036
W(3)—O(8)	0.1692	W(3)—O(8)	0.1784
W(3)—O(10)	0.2321	W(3)—O(10)	0.2427
W(3)—O(11)	0.1929	W(3)—O(11)	0.2036
W(3)—O(16)	0.1933	W(3)—O(16)	0.2036
W(4)—O(4)	0.1934	W(4)—O(4)	0.2036
W(4)—O(9)	0.1930	W(4)—O(9)	0.2037
W(4)—O(10)	0.2321	W(4)—O(10)	0.2423
W(4)—O(12)	0.1962	W(4)—O(12)	0.1784
W(4)—O(13)	0.1912	W(4)—O(13)	0.2036
W(4)—O(17)	0.1923	W(4)—O(17)	0.2038
W(5)—O(5)	0.1914	W(5)—O(5)	0.2037
W(5)—O(10)	0.2312	W(5)—O(10)	0.2425
W(5)—O(11)	0.1904	W(5)—O(11)	0.2037
W(5)—O(13)	0.1907	W(5)—O(13)	0.2036
W(5)—O(14)	0.1964	W(5)—O(14)	0.1783
W(5)—O(18)	0.1938	W(5)—O(18)	0.2036
W(6)—O(10)	0.2323	W(6)—O(10)	0.2426
W(6)—O(15)	0.1886	W(6)—O(15)	0.2036
W(6)—O(16)	0.1907	W(6)—O(16)	0.2036
W(6)—O(17)	0.1930	W(6)—O(17)	0.2037
W(6)—O(18)	0.1904	W(6)—O(18)	0.2036
W(6)—O(19)	0.1709	W(6)—O(19)	0.1783
W(1)—W(2)	0.328	W(1)—W(2)	0.343
W(1)—W(3)	0.328	W(1)—W(3)	0.343
W(1)—W(4)	0.329	W(1)—W(4)	0.343
W(1)—W(5)	0.328	W(1)—W(5)	0.343
W(1)—W(6)	0.465	W(1)—W(6)	0.343
W(2)—W(3)	0.328	W(2)—W(3)	0.343
W(3)—W(4)	0.327	W(3)—W(4)	0.343
W(4)—W(5)	0.328	W(4)—W(5)	0.343
W(5)—W(2)	0.327	W(5)—W(2)	0.343
W(6)—W(2)	0.328	W(6)—W(2)	0.343
W(6)—W(3)	0.329	W(6)—W(3)	0.343
W(6)—W(4)	0.328	W(6)—W(4)	0.343
W(6)—W(5)	0.328	W(6)—W(5)	0.343

[a]The figure shows the atomic labelling used in the table.

nent feature in each of the images is the pair of dark spots corresponding to a projection through two W_2 atom columns in the equatorial plane of the $[W_6O_{19}]^{2-}$ anion. Diffuse contrast due to the single axial W atoms in the anion substructure are also visible in the filtered image obtained from detail **I** (Figure 4a, right). In the filtered images corresponding to details **II** and **III**, only the lower atom is clearly visible (arrowed). None of these images show contrast obviously attributable to the $[nBu_4N]^+$ counterions owing to their weak contrast compared to the more strongly scattering objects in the specimen.

Line profiles (Figure 4b) obtained through the pairs of spots corresponding to the equatorial W_2 columns in the noise-filtered images reveal structural information about possible molecular relaxation and structural changes in the anion induced by the electron beam. The line profile obtained from **I** (after 50 s) indicates a maximum W_2 column separation of 0.39 nm, whereas profiles taken from **II** (after 60 s) and **III** (after 90 s) show progressively shorter W_2 column separations of 0.36 and 0.34 nm, respectively (estimated precision $\pm$ 0.02 nm). Comparing these distances with the corresponding W_2 column distances in the bulk crystal structure of $[W_6O_{19}][nBu_4N]_2$[36] shows an apparent expansion of the two pairs of W atoms in the equatorial plane of the anion relative to the bulk form (0.327 nm) as shown in Figure 4c. This indicates that the anion is relaxed in all three images but with a progressive contraction between the W_2 pair distances between images **I** to **III**. The progressive reduction in the W_2 separation (from 0.39 to 0.34 nm) may be attributed to gradual expulsion of O^{2-} from the $[W_6O_{19}]^{2-}$ anion during electron beam irradiation.

There are a number possible contributions to the apparent expansion of the $[W_6O_{19}]^{2-}$ anion observed

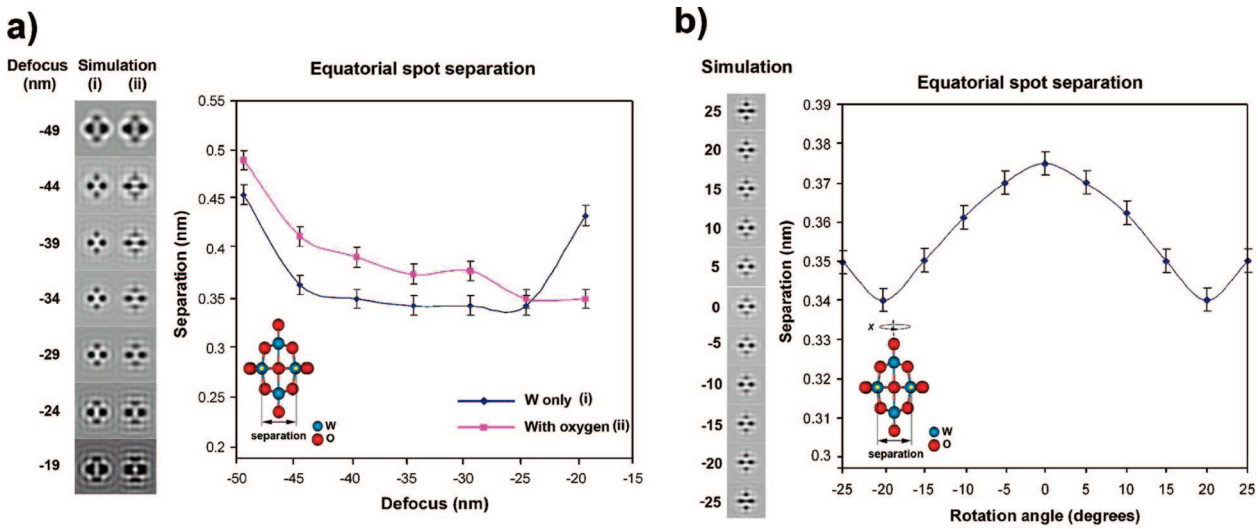

Figure 5. (a) HRTEM image simulations (left) and plot (right) showing the effect of including and excluding oxygens in the simulation of the $[W_6O_{19}]^{2-}$ anion at an *x*/*y* orientation (defined in Figures 1 and 2) of 45/0 as well as the effects of varying the objective lens defocus. (b) Image simulations (left) and plot (right) showing the effect of rotating the $[W_6O_{19}]^{2-}$ anion about the *x* axis starting from an *x*/*y* orientation (defined in Figures 1 and 2) of 45/0.

within the DWNT which may be attributed either to the structural behavior of the anion within the interior of the encapsulating nanotube or to the image contrast of the anion, taking into account the contribution of oxygen to the observed image contrast, the effect of defocus and the relative *x*/*y* orientation of the anion (defined in Figures 1 and 2) on the observed W_2 equatorial separation. The maximum relaxation that can be anticipated for the $[W_6O_{19}]^{2-}$ anion can be computed by relaxing the anion *in vacuo* relative to the anion as it exists in the bulk form,[36] as shown in Figure 4c. Relaxation of this structure *in vacuo* with MOPAC 7.1[47] using the PM6 parametrization for W and O and applying a net −2 charge to the W_6O_{19} species gives the relaxed bond distances in Figure 1c and in Table 1. For comparison, the corresponding unrelaxed bond distances from a single anion in the bulk crystal structure are reproduced in Figure 1c. In the relaxed anion, the separation of the two pairs of W atoms in the equatorial plane in projection is increased from 0.327 to 0.343 nm. Comparison of the calculated bond distances (Table 1) with the bulk structure bond distances shows that the relaxation causes a symmetrization of the bonds within the $[W_6O_{19}]^{2-}$ resulting in ideal O_h symmetry which is only approximated in the bulk form.

Distortion of the image contrast due to the O atoms in $[W_6O_{19}]^{2-}$ and the effects of objective lens defocus can also give rise to deviations in the observed W_2 equatorial spot separation which is best evaluated by HRTEM image simulation.[45,46] Comparing the image contrast of the $[W_6O_{19}]^{2-}$ anion at an *x*/*y* orientation of 45/0 computed at the Scherzer defocus with the oxygen atoms included (Figure 2d, left) and without the oxygen atoms (Figure 2d, right), shows that the centers of the W_2 equatorial spots are distorted outward toward the position of the three O_t oxygen atoms present on either side of the anion. This distortion can be seen by comparing the two simulations in which green crosses (W atom positions) and red crosses (O atom positions) have been added as a guide. In Figure 5a the effect of defocus on the W_2 equatorial spot separation is calculated, both with and without O included in the simulation, using the relaxed structure (*i.e.*, Figure 4c) as a starting point. Over a range of defoci from −40 to −25 nm which encompasses the Scherzer defocus value (−35 nm), the separation varies slightly from 0.39 to 0.375 nm. This compares to a W_2 equatorial column separation of 0.345−0.35 nm for the simulations calculated for the same defocus values but with only the W atoms included in the calculation. Outside this defocus window, the W_2 column separation varies markedly as the overall image contrast becomes more complex. A further contribution to the measured W_2 column separation may arise from a deviation from the 45/0 *x*/*y* orientation assumed for the anion (Figure 5b). Unlike the W_2 equatorial columns, there is relatively little distortion of the contrast around the apical W atoms by the surrounding O atoms (*cf.* Figure 4c,d). By varying the *x* angle and computing the equatorial W_2 column separation, it is apparent that rotating the $[W_6O_{19}]^{2-}$ anion about this axis causes a *decrease* in the W_2 spot separation from 0.375 nm at $x = 0°$ to 0.34 nm at $x = \pm 20°$. Overall from the combined experimental images and simulation data, we conclude that the observed W_2 equatorial spot expansion in the $[W_6O_{19}]^{2-}$ anion in images **I** and **II** is partly due to a relaxation of the anion within the DWNT and partly due to a distortion of the W_2 image contrast by the peripheral O_t oxygens attached to the equatorial W_2 atoms. In the case of image **III**, the observed W_2 relaxation is apparently lost, possibly due to the partial reduction of the anion and progressive expulsion of oxygen similar to

which we have previously reported for Re_xO_y clusters encapsulated within SWNTs.[48]

The separation of the apical distances within the anion (Figure 4a) is less easy to measure directly due to the diffuse contrast of single W atoms in the HRTEM images but varies from *ca*. 0.56 nm for image **I** (measured from both apical spots), to *ca.* 0.51 nm for image **II**, and *ca*. 0.58 nm for image **II** with the last two measurements being estimated from twice the distance of each lower spot to the plane defined by the pairs of W_2 atoms in images **II** and **III**. These compare to W−W apical atom separations (Figure 4c, see also Table 1) of 0.465 nm for the unrelaxed bulk anion and 0.485 nm for the MOPAC relaxed structure. Because of the low precision of the experimental measurements, it is difficult to be too confident about the precise W−W apical atom separations observed in Figure 4a but it is reasonable to conclude that the anions are relaxed along the apical plane also and may be expanded beyond the W−W distances calculated using MOPAC. Higher resolution images, possibly obtained at lower accelerating voltage may resolve this issue.

A noteworthy feature of the encapsulated $[W_6O_{19}]^{2-}$ species is its discontinuous motion between fixed locations along the length of the DWNT during irradiation (Figure 3a−f) and, in particular, that it locks into a fixed position (Figure 3 c−e) allowing the W_6 action template to be studied in some detail by HRTEM. In wider nanotubes, this regulated molecular motion is not observed and an irreversible agglomeration of clusters of $[W_6O_{19}][nBu_4N]_2$ (containing $[W_6O_{19}]^{2-)}$ is observed instead. In the sequence of six micrographs shown in Figure 6, two aggregates of $[W_6O_{19}][nBu_4N]_2$ can be seen (arrowed) rearranging and coalescing within a 1.45 nm diameter SWNT until a single large aggregate is observed (single arrow). These clusters were imaged under milder imaging conditions (120 kV accelerating voltage) than the conditions employed to image the discrete molecular anion shown in Figure 3a−f (300 kV accelerating voltage) but it is clear that this wider nanotube does not exert the same degree of control over the orientation and molecular motion of the encapsulated $[W_6O_{19}]^{2-}$ species. It is likely, in this instance, that the agglomeration of the $[W_6O_{19}][nBu_4N]_2$ is caused partly by gradual explusion of O^{2-} and is further facilitated by the absence of the steric influence of the narrower nanotube capillary.

The discontinuous motion of the encapsulated $[W_6O_{19}]^{2-}$ species observed in the narrower DWNT (Figure 3a−f) can be explained by considering the accommodation of the anion in the interior van der Waals surface of the host DWNT. Figure 7a illustrates that the "locked" $[W_6O_{19}]^{2-}$ anion is accommodated at an *x*/*y* = 45/0 and at an angle of *ca*. 60° to the tube growth axis (Figure 7b). The vertical cross-section of the nonspheroidal anion, once the radii of the O^{2-} coordinating anions (0.124 nm for O(II)) are taken into consideration, is *ca.* 0.96 nm (Figure 7b, right). If the innermost nanotube has a diameter of 1.21 nm (corresponding approximately to a (9,9) conformation SWNT, although the absolute (*n*,*m*) conformation[49–51] cannot be determined from the micrographs), then this will have an internal diameter of 0.87 nm once the van der Waals radii (0.17 nm) of the tube wall carbons are taken into consideration (Figure 7c,d). In this case the innermost nanotube will be too narrow by ~0.09 nm to accommodate the anion. This size difference may either be accommodated by the wall corrugation or by small asperities in the wall of the tubule. If we now consider the orthogonal horizontal cross-section of the anion within the tubule (Figure 7c), we see that it is easily accommodated by the innermost SWNT, being slightly smaller (0.84 nm) because of the nonspheroidal shape of the encapsulate (*cf*. encapsulated C_{60} and endofullerenes).[12–14] In the locked position, the anion will therefore have only one possible axis of rotation which will be parallel to the view direction in Figure 7d and through the center of gravity of the anion.

Given these steric constraints, an overall mechanism of translational motion for the anion along the

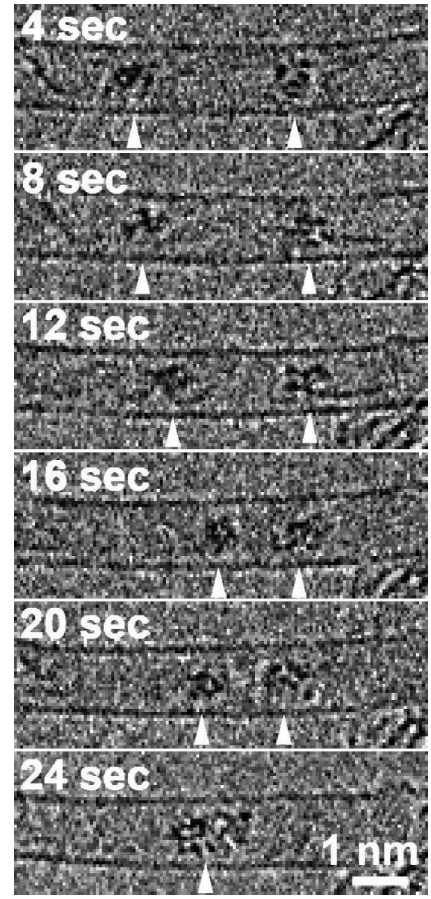

Figure 6. Sequence of six unprocessed HRTEM images recorded at 120 kV showing rotation and agglomeration of two groups of $[W_6O_{19}]^{2-}$ anions (probably stabilized by $[nBu_4N]^+$ counterions) in a relatively wide SWNT (1.45 nm diameter). During *ca.* 24 s beam exposure, the clusters rotate rapidly and eventually fuse to form a single agglomerate.

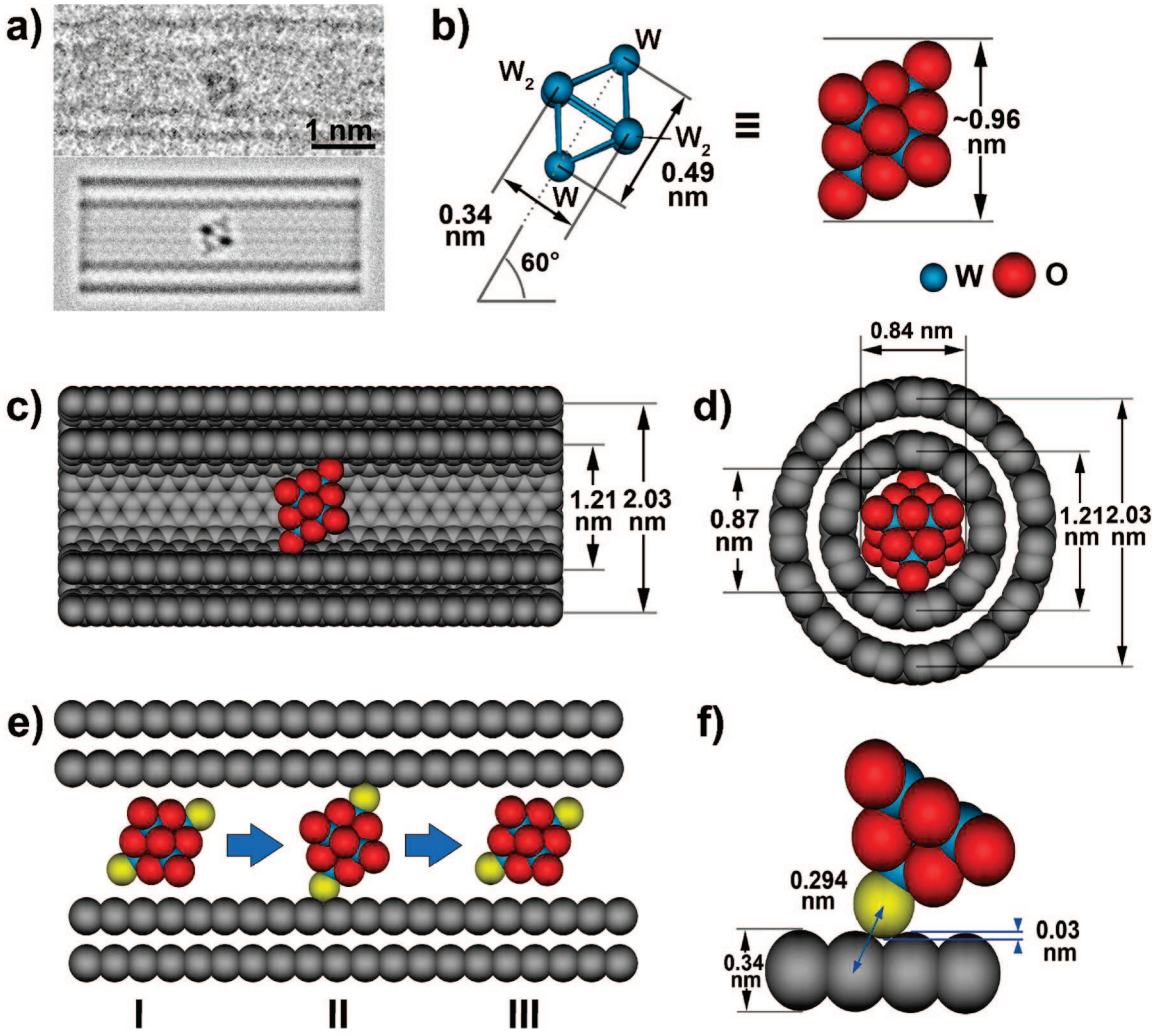

Figure 7. (a) Detail of a locked $[W_6O_{19}]^{2-}$ anion inside a DWNT obtained from an unprocessed HRTEM image (see also Figure 3c) shown together with an image simulation corresponding to a $[W_6O_{19}]^{2-}$@(9,9)@(14,14) SWNT pair. (b) Octahedral W_6 cation framework (left) and space-filling representation of a complete $[W_6O_{19}]^{2-}$ anion including O(II) (right). The indicated distance is the vertical cross-section of the cluster when W(VI) and O(II) radii are taken into account. (c) Cutaway side-on space-filling representation of the $[W_6O_{19}]^{2-}$:DWNT composite model (as used in the simulation in panel a). (d) End-on space-filling representation of the $[W_6O_{19}]^{2-}$@(9,9)@(14,14) SWNT composite with the internal diameter of the innermost (9,9) SWNT indicated, taking into account the 0.17 nm van der Waals radii of the C wall. (e) Schematic representation of a possible mechanism for translational motion of the $[W_6O_{19}]^{2-}$ anion within a DWNT. An unlocked anion translates from position I, rotates clockwise (~30°) about the one remaining degree of freedom and then "locks in" at position II. The anion can then unlock and translate further down the DWNT (III). The O^{2-} atoms in contact with the wall are indicated in yellow. (f) Diagram showing the 0.03 nm corrugation of the SWNT wall and minimum C−O distance in a locked in $[W_6O_{19}]^{2-}$ anion. The O^{2-} atom in contact with the wall is indicated in yellow.

capillary is proposed as shown in the idealized schematic in Figure 7e in which an unlocked anion located at position **I** translates to a second position at **II**, and then "locks in" by rotating about the one remaining degree of freedom. The anion can then move from this position by unlocking and translating (**III**) and so on. This particular mode of molecular motion may possibly be facilitated by the corrugation of the graphene wall of the encapsulating tubule, (Figure 7f), in which the ~0.03 nm dip at the centers of the carbon hexagons may accommodate the small excess in the vertical cross-section of the anion. An alternative explanation is that the effective increase in the steric cross-section of the anion may be accommodated by small asperities or bends in the wall carbon surface rather than by a wall corrugation. However we note that in both instances, the mode of translation is sterically restrained by the van der Waals surface of the enapsulating DWNT. The form of the molecular motion suggested here bears some similarity to a "molecular ratchet"[52] which has occasionally been observed in biological systems, for example in the transport of activated collagenase molecules (MMP-1) along collagen fibrils[53] and in man-made molecular systems, such as the rotary molecular motion described in triptycl[4]helicene.[54]

It is useful to consider our results in the light of recent investigations desribing the rapid transport properties of various gases and solutes through carbon nan-

otubes and nanotubes embedded in membranes. For example, Skouladis *et al*. have produced simulations of rapid transport of H_2 and CH_4 through defect-free SWNTs, predicting diffusion rates orders of magnitude higher than for zeolites of comparable pore sizes, behavior attributed to the "flat" potential energy surface (PES) of the tubules.[55] The same group also modeled enhanced transport properties for diffusion of N_2 and CH_4 through SWNTs embedded in membranes.[56] Subsequently Hinds *et al*.[57] produced experimental results demonstrating rapid diffusion of N_2 gas and also $Ru(NH_3)_6^+$ in solution through aligned MWNT membranes while Holt *et al*.[58] have also described the diffusion of gaseous species including H_2, He, N_2, O_2, Ar, CO_2, CH_4, and C_4H_8, solutes including $Ru^{2+}(bipyr)_3$ and Au colloids through aligned DWNT and MWNT membranes. Nearly all the species addressed in these studies are significantly smaller in external volume than the internal PES of the host nanotube and diffusion is therefore not sterically constrained as we have clearly observed for $[W_6O_{19}]^{2-}$ in the present work. An exception to this is described in the work Holt *et al*.[58] in which the diffusion/nondiffusion of Au colloids was used to gauge the size of the pores in DWNT membranes, estimated to be 1.3−2 nm based on the exclusion of colloids with a diameter greater than 2 nm (±0.4 nm). This work, however, still does not address the limiting case where the external surface of the diffusing species is sterically almost identical to the interface surface of the host nanotube as we have described for $[W_6O_{19}]^{2-}$ in the present study. This problem has been partly addressed in similar work on the diffusion of C_{60} molecules through SWNTs by Berber *et al*.[59] who modeled porous nanotubes with an atomically flat PES of similar steric size to the guest molecules. The ability of the latter to diffuse into porous SWNTs was partly controlled by the kinetic energy of the molecules with the result that efficient diffusion occurred at *ca*. 400 °C. Diffusion/molecular motion of C_{60} molecules and other fullerenes/endofullerenes at room temperature is clearly sterically hindered, however due to the demonstrated ease of observation of these species by HRTEM.[12−15] The presence of a "flat" PES on the internal surface of a carbon nanotube also does not necessarily preclude the "locking-in" mechanism which we have suggested because, as Skouladis *et al*. have noted: "We have considered only defect free nanotubes in our calculations. The presence of defects in the nanotubes (heteroatoms, holes, etc.) may have a profound effect on molecular diffusion by adding *corrugation* (our italics) to the molecule-solid PES."[55]

In the same context as the above, we should finally comment as to the likely role of the $[n\mathrm{Bu}_4\mathrm{N}]^+$ counterions in terms of stabilizing the observed $[W_6O_{19}]^{2-}$@DWNT/$[W_6O_{19}]^{2-}$@SWNT composites and in moderating the observed molecular motion and anion relaxation. However, at the present time, it is not possible to do more than speculate as to what this might be as, owing to their effective invisibility in the HRTEM images. Thus we do not know if the counterions are located in close proximity to the $[W_6O_{19}]^{2-}$ anion, or if they are located on the inside of the DWNTs (this seems likely in the case of the $[W_6O_{19}]^{2-}$ agglomerates in Figure 6), or are located on the exterior of the nanotube, or are on the interior of the nanotubes but located some distance away from the anions. These are all subjects for future investigation.

CONCLUSIONS

Polyoxometalate Lindqvist ions have been directly imaged within DWNTs and SWNTs by HRTEM for the first time, arguably the smallest 3D objects successfully characterized by this method. The constituent octahedral W_6 cation framework of a discrete $[W_6O_{19}]^{2-}$ anion has been resolved and relatively high precision structural information obtained about it with the caveat that the contrast of all the contribution constituent atoms should be taken into account. Prolonged electron beam irradiation of these species resulted in translational molecular motion that was sterically modulated by the internal surface of the encapsulating nanotube as a result of the nonspheroidal shape of the anion. Given the enormous variety of polyoxometalate compounds which can be prepared (which include larger and smaller substituted and derivatized molecular anions), there is considerable scope for further development of observation of similar molecular transport phenomenon and related structural studies within carbon nanotubes of varying diameters. With the advent of new C_s-corrected microscopes operated at lower voltages with superior resolution, it should be possible to study such single molecule species with increased precision and establish, for example, the precise structural relationships between the encapsulated anions and their host nanotubes. Improved resolution should also yield information about the counterion and its contribution to stabilizing the polyoxometalate-nanotube composites.

EXPERIMENTAL SECTION

Synthesis of DWNTs, SWNTs, and $[nBu_4N]_2[W_6O_{19}]$. The DWNTs used in these experiments were prepared by passing a mixture of H_2 and CH_4 (18 mol %) over a $Mg_{0.99}Co_{0.0075}Mo_{0.0025}O$ catalyst mixture at 1000 °C according to a published procedure.[60] The product was purified from extraneous oxide material and residual metal particles by soaking in concentrated aqueous HCl solution. SWNTs were prepared by a modified electric arc-evaporation technique.[61,62] $[n\mathrm{Bu}_4\mathrm{N}]_2[W_6O_{19}]$ was prepared according to a published procedure.[36] A 3.3g portion of $Na_2WO_4 \cdot H_2O$ was stirred with 4 mL of acetic anhydride and 3 mL of DMF at 100 °C for 3 h; 20 mL of acetic anhydride

was added to this creamy fluid and 1.8 mL of 12 M HCl in 5 mL of DMF was then added with further stirring. The hot suspension was gravity filtered to remove undissolved white solid. This was washed with 5 mL of MeOH and cooled to room temperature. A 1.5g portion of nBu$_4$NBr dissolved in 5 mL of MeOH was then added with rapid stirring for 5 min to give a white precipitate, which was then filtered using Whatman cyclopore 1 μm track-etched membranes to isolate the solid, and the precipitate was then washed with a small amount of MeOH and Et$_2$O. The resulting powder was then recrystallized from 1 mL of hot DMSO (80 °C). The solution was left to cool at room temperature for 2 days, over which small diamond shaped crystals were formed that were then filtered under suction. The structural identity of the [nBu$_4$N]$_2$[W$_6$O$_{19}$] was confirmed by XRD and comparison with the published structure.[36]

Filling of DWNTs and SWNTs. Filling of the treated DWNTs and SWNTs with [nBu$_4$N]$_2$[W$_6$O$_{19}$] was achieved using the "nanoextraction" technique described previously[44] in which preopened nanotubes were filled with endofullerenes by immersing them in saturated solutions of the target molecule. As [nBu$_4$N]$_2$[W$_6$O$_{19}$] is sparingly soluble in ethanol, a saturated solution of this was used to fill as-prepared DWNTs or SWNTs that had been preheated in dry air at 420 °C for 30 min. Crystals of [nBu$_4$N]$_2$[W$_6$O$_{19}$] were ground together with DWNTs or SWNTs and then stirred in solvent at 78 °C under reflux overnight. The suspension was filtered under suction using Whatman cyclopore 1 μm track-etched membranes and dried for 2 h at 110 °C.

HRTEM and Image Simulation. [nBu$_4$N]$_2$[W$_6$O$_{19}$]-filled DWNTs were examined at 300 kV in a JEOL JEM-3000F field emission gun HRTEM (C_3 = 0.6 nm). Unprocessed images were acquired at a magnification of 600000× on a Gatan model 794 (1024 × 1024 pixel) CCD camera for which the magnification was calibrated with MgO [111] lattice spacings recorded at the same time. The CCD pixellation error at 600 k is estimated to be *ca.* ± 0.02 nm. Image simulations were carried out using the multislice algorithm[45,46] using parameters typical for this instrument (coefficient of spherical aberration (C_3) = 0.6 mm, accelerating voltage 300 kV). Images of [nBu$_4$N]$_2$[W$_6$O$_{19}$]-filled SWNTs were obtained on both the JEOL JEM-3000F HRTEM and also a JEOL 2010F fitted with a CEOS aberration corrector operated at 120 kV. For this latter instrument C_3 was tuned to 0.001 mm.

Molecular Modeling. Single molecule fragments of W$_6$O$_{19}$ were extracted from the published crystal structure[36] and then relaxed *in vacuo* using the MOPAC 7.1 progam[47] using the PM6 parametrization for W and O. A charge of −2 was applied to the anion which could be relaxed efficiently within about 2 min on a desktop computer equipped with a 2 GHz Intel processor. Selected relaxed bond distances are reproduced in Figure 4c and in Table 1. Additional measurements were performed with the aid of the commercially available CrystalMaker software and standard Shannon anion and cation radii. Nanotube models were generated using the program Nanotube Modeler from JCrystalSoft (2004−2005).

Acknowledgment. We are indebted to C. Salzmann for assistance with the resynthesis of [nBu$_4$N]$_2$[W$_6$O$_{19}$] and to S. Llewellyn, A. Vlandas, and M. L. H. Green. We are also indebted to Dr. Andrew Cowley of the Chemistry Research Laboratory, Oxford, for assistance with the XRD characterization of [nBu$_4$N]$_2$[W$_6$O$_{19}$]. J.S. is indebted to the Royal Society for a University Research Fellowship, to the AIST for additional financial support and also to the Department of Materials, Oxford, for access to HRTEM facilities. J.S. and A.I.K. acknowledge financial support from the EPSRC (Grant No. GR/S83968/01). J.S. and E.F. acknowledge the CNRS and the Royal Society for a Joint Project Grant (Grant No. 15410). We thank one of the referees for prompting us to include in this paper a discussion of our results in the context of molecular diffusion in various nanotubes and nanotube membranes.

REFERENCES AND NOTES

1. Fan, X.; Dickey, E. C.; Eklund, P. C.; Williams, K. A.; Grigorian, L.; Buczko, R.; Pantelides, S. T.; Pennycook, S. J. Reversible Intercalation of Charged Iodine Chains into Carbon Nanotube Ropes. *Phys. Rev. Lett.* **2000**, *84*, 4621–4624.
2. Guan, L.; Suenaga, K.; Zujin, S.; Gu, Z.; Iijima, S. Atomic Chains of Iodine and their Phase Transition in Confined Nanospace. *Nano Lett.* **2007**, *7*, 1532–1535.
3. Sloan, J.; Novotny, M. C.; Bailey, S. R.; Brown, G.; Xu, C.; Williams, V. C.; Friedrichs, S.; Flahaut, E.; Callendar, R. L.; York, A. P. E.; et al. Two Layer 4:4 Co-ordinated KI Crystals Grown Within Single Walled Carbon Nanotubes. *Chem. Phys. Lett.* **2000**, *29*, 61–65.
4. Meyer, R. R.; Sloan, J.; Dunin-Borkowski, R. E.; Novotny, M. C.; Bailey, S. R.; Hutchison, J. L.; Green, M. L. H. Discrete Atom Imaging of One-Dimensional Crystals Formed Within Single-Walled Carbon Nanotubes. *Science* **2000**, *289*, 1324–1326.
5. Xu, C.; Sloan, J.; Brown, G.; Bailey, S. R.; Williams, V. C.; Friedrichs, S.; Coleman, K. S.; Hutchison, J. L.; Dunin-Borkowski, R. E.; Green, M. L. H. 1D Lanthanide Halide Crystals Inserted into Single-Walled Carbon Nanotubes. *Chem. Commun.* **2000**, *242*, 7–2428.
6. Satishkumar, B. C.; Taubert, A.; Luzzi, D. E. Filling Single Wall Carbon Nanotubes with d- and f-Metal Chloride and Metal Nanowires. *J. Nanosci. Nanotechnol.* **2003**, *3*, 159–163.
7. Maniwa, Y.; Kataura, Abe. M.; Suzuki, S.; Achiba, Y.; Kira, H.; Matsuda, K. Phase Transition in Confined Water Inside Carbon Nanotubes. *J. Phys. Soc. Jpn.* **2002**, *71*, 2863–2866.
8. Kolesnikov, A. I.; Zanotti, J. M.; Loong, C. K.; Thiyagarajan, P.; Moravsky, A. P.; Loutfy, R. O.; Burnham, C. J. Multi-Wall Ice Helices and Ice Nanotubes. *Phys. Rev. Lett.* **2004**, *93*, 0355031–4.
9. Philp, E.; Sloan, J.; Kirkland, A.I.; Meyer, R. R.; Friedrichs, S.; Hutchison, J. L.; Green, M. L. H. An Encapsulated 1D Cobalt Iodide Crystal. *Nat. Mater.* **2003**, *2*, 788–791.
10. Carter, R.; Sloan, J.; Vlandas, A.; Green, M. L. H.; Kirkland, A. I.; Meyer, R. R.; Hutchison, J. L.; Lindan, P. J. D.; Lin, G.; Harding, J. Correlation of Structural and Electronic Properties in a New Low Dimensional Form of Mercury Telluride. *Phys. Rev. Lett.* **2006**, *96*, 215501/1–4.
11. Flahaut, E.; Sloan, J.; Friedrichs, S.; Kirkland, A. I.; Coleman, K. S.; Williams, V. C.; Hanson, N.; Hutchison, J. L.; Green, M. L. H. Crystallisation of 2H and 4H PbI$_2$ in Carbon Nanotubes of Varying Diameters and Morphologies. *Chem. Mater.* **2006**, *18*, 2059–2069.
12. Smith, B. W.; Monthioux, M.; Luzzi, D. E. Encapsulated C$_{60}$ in Carbon Nanotubes. *Nature* **1998**, *396*, 323–324.
13. Smith, B. W.; Luzzi, D. E.; Achiba, Y. Tumbling Atoms and Evidence for Charge Transfer in La$_2$@C$_{80}$@SWNT. *Chem. Phys. Lett.* **2000**, *331*, 137–142.
14. Suenaga, K.; Tence, M.; Mory, C.; Colliex, C.; Kato, H.; Okazaki, T.; Shinohara, H.; Hirahara, K.; Bandow, S.; Iijima, S. Element Selective Single Atom Imaging. *Science* **2000**, *290*, 2280–2282.
15. Liu, Z.; Koshino, M.; Suenaga, K.; Mrzel, A.; Kataura, H.; Iijima, S. Transmission Electron Microscopy Imaging of Individual Functional Groups of Fullerene Derivatives. *Phys. Rev. Lett.* **2006**, *96*, 088304/1–4.
16. Lu, J.; Nagase, S.; Yu, D.; Ye, H.; Han, R,; Gao, Z.; Zhang, S.; Peng, L. Amphoteric and Controllable Doping of Carbon Nanotubes by Encapsulation of Organic and Organometallic Molecules. *Phys. Rev. Lett.* **2004**, *93*, 116804/1–4.
17. Li, L-J.; Khlobystov, A. N.; Wiltshire, J. G.; Briggs, G. A. D.; Nicholas, R. J. Diameter-Selective Encapsulation of Metallocenes in Single-Walled Carbon Nanotubes. *Nat. Mater.* **2005**, *4*, 481–485.
18. Guan, L.; Shi, Z.; Li, M.; Gu, Z. Ferrocene Filled Single Walled Carbon Nanotubes. *Carbon* **2005**, *43*, 2780–2785.
19. Kataura, H.; Maniwa, Y.; Abe, M.; Fujiwara, A.; Kodama, T.; Kikuchi, K.; Imahori, H.; Misaki, Y.; Suzuki, S.; Achiba, Y. Optical Properties of Fullerene and Non-Fullerene Peapods. *Appl. Phys. A: Mater. Sci. Process.* **2002**, *74*, 349–354.
20. Morgan, D. A.; Sloan, J.; Green, M. L. H. Direct Imaging of *o*-Carborane Molecules Within Single Walled Carbon Nanotubes. *Chem. Commun.* **2002**, 2442–2443.

21. Thamavaranukup, N.; Höppe, H. A.; Ruiz-Gonzalez, L.; Costa, P.; Sloan, J.; Kirkland, A. I.; Green, M. L. H. Single-Walled Carbon Nanotubes Filled with *M*OH (*M* = K, Cs) and Then Washed and Refilled with Molecules and Clusters. *Chem. Commun.* **2004**, 1686–1687.
22. Khlobystov, A. N.; Britz, D. A.; Briggs, G. A. D. Molecules in Carbon Nanotubes. *Acc. Chem. Res.* **2005**, *38*, 901–909.
23. Coene, W.; Janssen, G.; Op de Beeck, M.; van Dyck, D. Phase Retrieval Through Focus Variation for Ultra-Resolution in Field-Emission Transmission Electron Microscopy. *Phys. Rev. Lett.* **1992**, *69*, 3743–3746.
24. van Dyck, D.; Op de Beeck, M.; Coene, W. A New Approach to Object Wave-Function Reconstruction in Electron Microscopy. *Optik* **1993**, *93*, 103–107.
25. Coene, W.; Thust, A.; Op de Beeck, M.; van Dyck, D. Maximum-Likelihood Method for Focus-Variation Image Reconstruction in High Resolution Transmission Electron Microscopy. *Ultramicroscopy* **1996**, *64*, 109–135.
26. Meyer, R. R.; Kirkland, A. I.; Saxton, W. O. A New Method for the Determination of the Wave Aberration Function for High Resolution TEM. 1. Measurement of the Symmetric Abberations. *Ultramicroscopy* **2002**, *92*, 89–109.
27. Haider, M.; Uhlemann, S.; Schwan, E. Electron Microscopy Image Enhanced. *Nature* **1998**, *392*, 768–760.
28. David, W. I. F.; Iberrson, R. M.; Matthewman, J. C.; Prassides, K.; Dennis, T. J. S.; Hare, J. P.; Kroto, H. W.; Taylor, R.; Walton, D. R. M. Crystal Structure and Bonding of Ordered C_{60}. *Nature* **1991**, *353*, 147–149.
29. Pope, M. T.; Müller, A. Polyoxometalate Chemistry: An Old Field with New Dimensions in Several Disciplines. *Angew. Chem. Int. Ed.* **1991**, *30*, 34–38.
30. Hill, C. L.; Prosser-McCartha, C. M. Homogeneous Catalysis by Transition Metal Oxygen Anion Clusters. *Coord. Chem. Rev.* **1995**, *143*, 407–455.
31. Rhule, J. T.; Hill, C. L.; Judd, D. A.; Schinazi, R. F. Polyoxometalates in Medicine. *Chem. Rev.* **1998**, *98*, 327–358.
32. Klemperer, W.; Wall, C. Polyoxoanion Chemistry Moves Toward the Future: From Solids and Solutions to Surfaces. *Chem. Rev.* **1998**, *98*, 297–306.
33. Lüpez, X.; Nieto-Draghi, C.; Bo, C.; Avalos, J. B.; Poblet, J. M. Polyoxometalates in Solution: Molecular Dynamics Simulations on the α-$PW_{12}O_{40}^{3-}$ Keggin Anion in Aqueous Media. *J. Phys. Chem. A* **2005**, *109*, 1216–1222.
34. Ruhlmann, L.; Genet, G. Wells-Dawson-Derived Tetrameric Complexes ($K_{28}H_8$ $[P_2W_{15}Ti_3O_{60.5}]_4$) Electrochemical Behaviour and Electrocatalytic Reduction of Nitrite and of Nitric Oxide. *J. Electroanal. Chem.* **2004**, *568*, 315–321.
35. Alizadeh, M. H.; Harmalker, S. P.; Jeannin, Y.; Martin-Frere, J.; Pope, M. T. A Heteropolyanion with Fivefold Molecular Symmetry that Contains a Nonlabile Encapsulated Sodium Ion. The Structure and Chemistry of $[NaP_5W_{30}O_{11}0]^{14-}$. *J. Am. Chem. Soc.* **1985**, *107*, 2662–2669.
36. Fuchs, J.; Freiwald, W.; Hartle, H. Neubestimmung der Kristallstruktur von Tetrabutylammoniumhexawolframat. *Acta Crystallogr.* **1978**, *B34*, 1764–1770.
37. Volkmer, D.; Bredenkötter, B.; Tellenbröker, J.; Kögerler, P.; Kurth, D. G.; Lehmann, P.; Schnablegger, H.; Schwahn, D.; Pipenbrink, M.; Krebs, B. Structure and Properties of the Dendron-Encapsulated Polyoxometalate $(C_{52}H_{60}NO_{12})_{12}[(Mn(H_2O))_3(SbW_9O_{33})_2]$, a First Generation Dendrizyme. *J. Am. Chem. Soc.* **2002**, *124*, 10489–10496.
38. Sarafianos, S. G.; Kortz, U.; Pope, M. T.; Modak, M. J. Mechanism of Polyoxometalate-Mediated Inactivation of DNA Polymerases: an Analysis with HIV-1 Reverse Transcriptase Indicates Specificity for the DNA-Binding Cleft. *Biochem. J.* **1996**, *319*, 619–626.
39. Kozhenvikov, I. V. Catalysis by Heteropoly Acids and Multicomponent Polyoxometalates in Liquid-Phase Reactions. *Chem. Rev.* **1998**, *98*, 171–198.
40. Clemente-Juan, J. M.; Coronado, E.; Galán-Mascarüs, J. J. R.; Gümez-Garciá, C. J. Increasing the Nuclearity of Magnetic Polyoxometalates. Syntheses, Structures, and Magnetic Properties of Salts of the Heteropoly Complexes $[Ni_3(H_2O)_3(PW_{10}O_{39})H_2O]^{7-}$, $[Ni_4(H_2O)_2(PW_9O_{34})_2]^{10-}$, and $[Ni_9(OH)_3(H_2O)_6(HPO_4)_2(PW_9O_{34})_3]^{16-}$. *Inorg. Chem.* **1999**, *38*, 55–63.
41. Lehmann, J.; Gaita-Arino, A.; Coronado, E.; Loss, D. Spin Qubits with Electrically Gated Polyoxometalate Molecules. *Nat. Nanotechnol.* **2007**, *5*, 312–317.
42. Linqvist, I. On the Structure of the Hexaniobate Anion. *Ark. Kemi.* **1952**, *5*, 247–250.
43. Linqvist, I.; Aronsson, B. The Crystal Structure of the Hexatantalate Anion. *Ark. Kemi* **1954**, *7*, 49–52.
44. Yudasaka, M.; Ajima, K.; Suenaga, K.; Ichihashi, T.; Hashimoto, A.; Iijima, S. Nano-Extraction and Nano-Condensation for C_{60} Incorporation into Single-Wall Carbon Nanotubes in Liquid Phases. *Chem. Phys. Lett.* **2003**, *380*, 42–46.
45. Cowley, J. M.; Moodie, A. F. The Scattering of Electrons by Atoms and Crystals. I. A New Theoretical Approach. *Acta Crystallogr.* **1957**, *10*, 609–619.
46. Goodman, P.; Moodie, A. F. Numerical Evaluations of N-beam Wave Functions in Electron Scattering by the Multi-Slice Method. *Acta Cryst.* **1974**, *A30*, 280–290.
47. Stewart, J. *MOPAC 7.1*; 15210 Paddington Circle, Colorado Springs, CO 80921.
48. Costa, P. M. F. J.; Sloan, J.; Rutherford, T.; Green, M. L. H. Encapsulation of Re_xO_y Clusters within Single Walled Carbon Nanotubes and their *In-Tubulo* Reduction and Sintering to Re Metal. *Chem. Mater.* **2005**, *17*, 6579–6582.
49. Saito, R.; Fujita, G.; Dresselhaus, M. S.; Dresselhaus, G. Electronic Structure of Chiral Graphene Tubules. *Appl. Phys. Lett.* **1992**, *60*, 2204–2206.
50. Dresselhaus, M. S.; Dresselhaus, G.; Eklund, P. C. Physics of Carbon Nanotubes. *Carbon* **1995**, *33*, 883–891.
51. Meyer, R. R.; Friedrichs, S.; Kirkland, A. I.; Sloan, J.; Hutchison, J. L.; Green, M. L. H. A Composite Method for the Determination of the Chirality of Single-Walled Carbon Nanotubes. *J. Microsc.* **2003**, *212*, 152–157.
52. Feynman, R. P.; Leighton, R. B.; Sands, M. In *The Feynman Lectures on Physics*; Addison-Wesley: Reading, MA, 1963; Vol. 1, Chapter 46.
53. Saffarian, S.; Collier, I. E.; Marmer, B. L.; Elson, E. L.; Goldberg, G. Interstitial Collagenase is a Brownian Ratchet Driven by Proteolysis of Collagen. *Science* **2004**, *306*, 108–111.
54. Ross Kelly, T.; De Silva, H.; Silva, R. A. Unidirectional Rotary Motion in a Molecular System. *Nature* **1999**, *401*, 150–152.
55. Skoulidas, A. I.; Ackerman, D. M.; Scholl, D. S.; Johnson, J. K. Rapid Transport of Gases in Carbon Nanotubes. *Phys. Rev. Lett.* **2002**, *89*, 185901/1–4.
56. Skoulidas, A. I; Scholl, D. S.; Johnson, J. K. Adsorption and Diffusion of Carbon Dioxide and Nitrogen Through Single-Walled Carbon Nanotube Membranes. *J. Chem. Phys.* **2006**, *124*, 054708/1–7.
57. Hinds, B. J.; Chopra, N.; Rantell, T.; Andrews, R.; Gavalas, V.; Bachas, L. G. Aligned Multiwalled Carbon Nanotube Membranes. *Science* **2004**, *303*, 62–65.
58. Holt, K.; Park, H. G.; Wang, Y.; Stadermann, M.; Artyukhin, A. B.; Grigoropoulos, C. P.; Noy, A.; Bakajin, O. Fast Mass Transport Through Sub-2-Nanometer Carbon Nanotubes. *Science* **2006**, *312*, 1034–1037.
59. Berber, S.; Kwon, Y. K.; Tománek, D. Microscopic Formation Mechanism of Nanotube Peapods. *Phys. Rev. Lett.* **2002**, *88*, 185502/1–4.
60. Flahaut, E.; Bacsa, R.; Peigney, A.; Laurent, C. Gram-Scale CCVD Synthesis of Double-Walled Carbon Nanotubes. *Chem. Commun.* **2003**, 1442–1443.
61. Krätschmer, W.; Lamb, L. D.; Fostiropoulos, K.; Huffman, D. R. Solid C_{60}: A New Form of Carbon. *Nature* **1990**, *347*, 354–358.
62. Journet, C.; Maser, W. K.; Bernier, P.; Loiseau, A.; Lamy de la Chapelle, M.; Lefrant, S.; Deniard, P.; Lee, R.; Fischer, J. E. Large-Scale Production of Single-Walled Carbon Nanotubes by the Electric-Arc Technique. *Nature* **1997**, *388*, 756–758.